Article

Synthesis of Chiral Self-Assembling Rhombs and Their Characterization in Solution, in the Gas Phase, and at the Liquid–Solid Interface

Kyung Seok Jeong, Sun Young Kim, Ueon-Sang Shin, Michael Kogej, Nguyen T. M. Hai, Peter Broekmann, Nakcheol Jeong, Barbara Kirchner, Markus Reiher, and Christoph A. Schalley

J. Am. Chem. Soc., **2005**, 127 (50), 17672-17685• DOI: 10.1021/ja053781i • Publication Date (Web): 24 November 2005

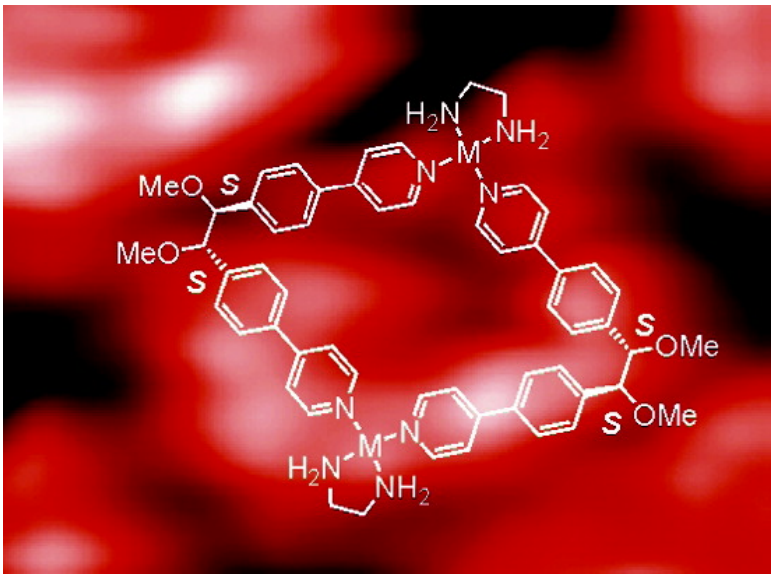

More About This Article

Additional resources and features associated with this article are available within the HTML version:

- Supporting Information
- Links to the 16 articles that cite this article, as of the time of this article download
- Access to high resolution figures
- Links to articles and content related to this article
- Copyright permission to reproduce figures and/or text from this article

View the Full Text HTML

J|A|C|S
ARTICLES
Published on Web 11/24/2005

Synthesis of Chiral Self-Assembling Rhombs and Their Characterization in Solution, in the Gas Phase, and at the Liquid−Solid Interface

Kyung Seok Jeong,[†] Sun Young Kim,[†] Ueon-Sang Shin,[†] Michael Kogej,[‡] Nguyen T. M. Hai,[§] Peter Broekmann,*[,§] Nakcheol Jeong,*[,†] Barbara Kirchner,*[,§] Markus Reiher,*[,⊥] and Christoph A. Schalley*[,‡]

Contribution from the Department of Chemistry and Division of Molecular Engineering and Chemistry, Korea University, Seoul, 136-701, Korea, Institut für Physikalische und Theoretische Chemie, Universität Bonn, Wegelerstrasse 12, D-53115, Bonn, Germany, Institut für Chemie und Biochemie−Organische Chemie, Freie Universtät Berlin, Takustrasse 3, D-14195, Berlin, Germany, and Institut für Physikalische Chemie, Universität Jena, Helmholtzweg 4, D-07743, Jena, Germany

Received June 9, 2005; Revised Manuscript Received October 18, 2005; E-mail: broekman@thch.uni-bonn.de; njeong@korea.ac.kr; kirchner@thch.uni-bonn.de; markus.reiher@uni-jena.de; schalley@chemie.fu-berlin.de

Abstract: Chiral, enantiopure metallo-supramolecular rhombs self-assemble in solution through coordination of bis-pyridyl-substituted ligands with (en)$M(NO_3)_2$ (en = ethylenediamine, M = Pd^{II}, Pt^{II}). Characterization by NMR and CD spectroscopy in solution and by ESI-FT-ICR mass spectrometry in the gas phase suggests that an equilibrium exists in water/methanol of a major 2:2 complex and a minor 3:3 complex of ligands and metal corners. In the gas phase, doubly charged 2:2 complexes fragment into two identical singly charged halves followed by metal-mediated C−H and C−C bond activation reactions within the ethylenediamine ligands. Electrochemical scanning tunneling microscopy (EC-STM) provides in situ imaging of the complexes even with submolecular resolution. Flat-lying rhombs are deposited under potential control from an aqueous electrolyte on a Cu(100) electrode surface precovered by a tetragonal pattern of chloride anions from the supporting electrolyte. Chirality induces the formation of only one domain orientation. Density functional calculations help to interpret the STM images.

Introduction

Self-assembly under thermodynamic control offers a convenient way to generate complex structures, in particular because error correction is ensured by their reversible formation.[1] The information governing the geometry of the final assembly is programmed into the individual building blocks through synthesis, e.g., through suitably positioned and complementary binding sites and the required rigidity of the subunits. Metallo-supramolecular systems[2] are particularly advantageous for self-assembly, because transition metals offer a large variety of different coordination geometries and sometimes even permit switching between geometries by changing the oxidation state.[3] Many reversible coordinative bonds are known that ensure error correction in the self-assembly process, and it is still a challenge to introduce chirality into such self-assembled species.[4]

Besides their successful synthesis and characterization, the implementation of function represents a major goal. Self-assembling polygons and polyhedra have been reported that can

[†] Korea University.
[‡] Freie Universtät Berlin.
[§] Universität Bonn.
[⊥] Universität Jena.

(1) For selected reviews, see: (a) Lindsey, J. S. *New J. Chem.* **1991**, *15*, 153−180. (b) Whitesides, G. M.; Mathias, J. P.; Seto, C. T. *Science* **1991**, *254*, 1312−1319. (c) Philp, D.; Stoddart, J. F. *Angew. Chem.* **1996**, *108*, 1242−1286; *Angew. Chem., Int. Ed. Engl.* **1996**, *35*, 1154−1196. (d) Schalley, C. A.; Lützen, A.; Albrecht, M. *Chem. Eur. J.* **2004**, *10*, 1072−1080. For a particular application of self-assembly to mesoscale objects, see: (e) Bowden, N. B.; Weck, M.; Choi, I. S.; Whitesides, G. M. *Acc. Chem. Res.* **2001**, *34*, 231−238.

(2) For reviews on polynuclear, self-assembling metal complexes, see: (a) Fujita, M. Self-assembled Macrocycles, Cages, and Catenanes Containing Transition Metals in Their Backbones. In *Comprehensive Supramolecular Chemistry*; Atwood, J. L., Davies, J. E. D., MacNicol, D. D., Vögtle, F., Lehn, J.-M., Sauvage, J.-P., Hosseini, M. W., Eds.; Pergamon: Oxford, 1996; Vol. 9, pp 253−282. (b) Fredericks, J. R.; Hamilton, A. D. Metal Template Control of Self-Assembly in Supramolecular Chemistry. In *Supramolecular Control of Structure and Reactivity—Perspectives in Supramolecular Chemistry*; Hamilton, A. D., Ed.; Wiley: New York, 1996; Vol. 3, pp 1−39. (c) Fujita, M. Ogura, K. *Coord. Chem. Rev.* **1996**, *148*, 249−264. (d) Fujita, M.; Ogura, K. *Bull. Chem. Soc. Jpn.* **1996**, *69*, 1471−1482. (e) Piguet, C.; Bernardinelli, G.; Hopfgartner, G. *Chem. Rev.* **1997**, *97*, 2005−2062. (f) Stang, P. J.; Olenyuk, B. *Acc. Chem. Res.* **1997**, *30*, 502−518. (g) Albrecht, M. *Chem. Soc. Rev.* **1998**, *27*, 281−287. (h) Jones, C. J. *Chem. Soc. Rev.* **1998**, *27*, 289−299. (i) Fujita, M. *Chem. Soc. Rev.* **1998**, *27*, 417. (j) Slone, R. V.; Benkstein, K. D.; Bélanger, S.; Hupp, J. T.; Guzei, I. A.; Rheingold, A. L. *Coord. Chem. Rev.* **1998**, *171*, 221−243. (k) Piguet, C. *J. Inclusion Phenom. Macrocyclic Chem.* **1999**, *34*, 361−391. (l) Caulder, D. L.; Raymond, K. N. *Acc. Chem. Res.* **1999**, *32*, 975−982. (m) Leininger, S.; Olenyuk, B.; Stang, P. J. *Chem. Rev.* **2000**, *100*, 853−908. (n) Fujita, M.; Umemoto, K.; Yoshizawa, M.; Fujita, N.; Kusukawa, T.; Biradha, K. *Chem. Commun.* **2001**, 509−518. (o) Holliday, B. J.; Mirkin, C. A. *Angew. Chem.* **2001**, *113*, 2076−2097; *Angew. Chem., Int. Ed.* **2001**, *40*, 2022−2043. (p) Albrecht, M. *Chem. Rev.* **2001**, *101*, 3457−3498. (q) Johnson, D. W.; Raymond, K. N. *Supramol. Chem.* **2001**, *13*, 639−659. (r) Swiegers, G. F.; Malfetse, T. J. *J. Inclusion Phenom. Macrocyclic Chem.* **2001**, *40*, 253−264. (s) Cotton, F. A.; Lin, C.; Murillo, C. A. *Acc. Chem. Res.* **2001**, *34*, 759−771. (t) Sun, S.-S.; Lees, A. J. *Coord. Chem. Rev.* **2002**, *230*, 171−192. (u) Würthner, F.; You, C.-C.; Saha-Möller, C. R. *Chem. Soc. Rev.* **2004**, *33*, 133−146. (v) Hofmeier, H.; Schubert, U. S. *Chem. Soc. Rev.* **2004**, *33*, 373−399.

10.1021/ja053781i CCC: $30.25

Chart 1. Enantiopure, Water-Soluble, Metallo-Supramolecular Rhombs (*S*,*S*,*S*,*S*)-**1a**,**b** and (*S*,*S*,*S*,*S*)-**2a**,**b** Generated through Self-Assembly[a]

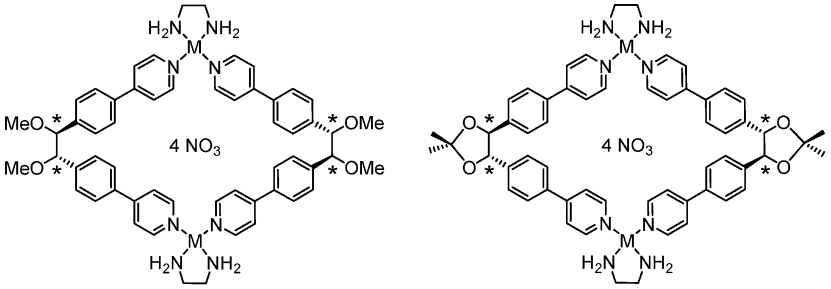

(*S*,*S*,*S*,*S*)-**1a** (M = Pd^{II})
(*S*,*S*,*S*,*S*)-**1b** (M = Pt^{II})

(*S*,*S*,*S*,*S*)-**2a** (M = Pd^{II})
(*S*,*S*,*S*,*S*)-**2b** (M = Pt^{II})

[a] For comparison, the corresponding enantiomers (*R*,*R*,*R*,*R*)-**1a**,**b** have also been prepared (not shown).

be used as hosts,[5] to control the stereochemistry of photochemical [2+2] cycloadditions,[6] and to catalyze reactions through encapsulation.[7] The generation of higher levels of order is mandatory, if macroscopic effects are to be achieved. One approach toward this goal is the ordered deposition of self-assembled species on surfaces[8] where they can be examined with scanning probe microscopy.[9] Recently, we[10] and Gong et al.[11] described experiments using highly ordered pyrolytic graphite (HOPG) and Cu(100) surfaces for the deposition of metallo-supramolecular squares and rectangles. When the interactions of the cationic metallo-supramolecular species with the surface were enhanced by depositing a tetragonal grid of chloride anions on Cu(100), the complexes deposit in a flat orientation and open their cavity toward the solution phase. One future goal is to use this arrangement of metallo-supramolecular macrocycles for a surface confined host−guest chemistry that can be directly visualized by means of in situ STM.[12] The electrochemical environment used in our STM experiments appears advantageous since external stimuli like potential-mediated electron-transfer reactions offer control[10c] over the reversible inclusion or the release of redox-active guests into adsorbed host assemblies.

In the present study, the synthesis of novel enantiopure, self-assembling rhombs is reported (Chart 1) followed by their characterization in solution by nuclear magnetic resonance (NMR) and circular dichroism (CD) spectroscopy and in the gas phase by electrospray ionization Fourier transform ion cyclotron resonance (ESI-FT-ICR) mass spectrometry. At the solid−liquid interface, individual rhombs are structurally characterized by electrochemical scanning tunneling microscopy (EC-STM). Quite intriguingly, the chirality of these rhombs is expressed in the long-range order on the chloride-modified

(3) Molecular muscles are one example, in which the coordination geometry of a copper ion is changed through redox processes and leads to mechanical motion: (a) Collin, J.-P.; Dietrich-Buchecker, C.; Gaviña, P.; Jimenez-Molero, M. C.; Sauvage, J.-P. *Acc. Chem. Res.* **2001**, *34*, 477−487. (b) Amendola, V.; Fabbrizzi, L.; Mangano, C.; Pallavicini, P. *Struct. Bonding (Berlin)* **2001**, *99*, 79−115. (c) Collin, J. P.; Gavina, P.; Heitz, V.; Sauvage, J. P. *Eur. J. Inorg. Chem.* **1998**, *1*, 1−14. (d) Livoreil, A.; Dietrich-Buchecker, C. O.; Sauvage, J.-P. *J. Am. Chem. Soc.* **1994**, *116*, 9399−9400. (e) Livoreil, A.; Armaroli, N.; Balzani, V.; Flamigni, B.; Ventura, B. *J. Am. Chem. Soc.* **1997**, *119*, 12114−12124. (f) Cárdenas, D. J.; Livoreil, A.; Sauvage, J.-P. *J. Am. Chem. Soc.* **1996**, *118*, 11980−11981.

(4) (a) Stang, P. J.; Olenyuk, B.; Muddiman, D. C.; Smith, R. D. *Organometallics* **1997**, *16*, 3094−3096. (b) Schweiger, M.; Seidel, S. R.; Schmitz, M.; Stang, P. J. *Org. Lett.* **2000**, *2*, 1255−1257. (c) Kubota, Y.; Biradha, K.; Fujita, M.; Sakamoto, S.; Yamaguchi, K. *Bull. Chem. Soc. Jpn.* **2002**, *75*, 559−565. (d) Müller, C.; Whiteford, J. A.; Stang, P. J. *J. Am. Chem. Soc.* **1998**, *120*, 9827−9837. (e) Stang, P. J.; Olenyuk, B.; Arif, A. M. *Organometallics* **1995**, *14*, 5281−5289.

(5) (a) Müller, I. M.; Möller, D.; Schalley, C. A. *Angew. Chem.* **2005**, *117*, 485−488; *Angew. Chem., Int. Ed.* **2005**, *44*, 480−484. (b) Brumaghim, J. L.; Michels, M.; Raymond, K. N. *Eur. J. Org. Chem.* **2004**, *22*, 4552−4559. (c) Fiedler, D.; Pagliero, D.; Brumaghim, J. L.; Bergman, R. G.; Raymond, K. N. *Inorg. Chem.* **2004**, *43*, 846−848. (d) Johnson, D. W.; Raymond, K. N. *Supramol. Chem.* **2001**, *13*, 639−659. (e) Johnson, D. W.; Raymond, K. N. *Inorg. Chem.* **2001**, *40*, 5157−5161. (f) Caulder, D. L.; Powers, R. E.; Parac, T. N.; Raymond, K. N. *Angew. Chem.* **1998**, *110*, 1940−1943; *Angew. Chem., Int. Ed.* **1998**, *37*, 1840−1843.

(6) Yoshizawa, M.; Takeyama, Y.; Kusukawa, T.; Fujita, M. *Angew. Chem.* **2002**, *114*, 1403−1405; *Angew. Chem., Int. Ed.* **2002**, *41*, 1347−1349.

(7) Selected examples for catalysis in capsules: (a) Kusukawa, T.; Nakai, T.; Okano, T.; Fujita, M. *Chem. Lett.* **2003**, *32*, 284−285. (b) Fiedler, D.; Bergman, R. G.; Raymond, K. N. *Angew. Chem.* **2004**, *116*, 6916−6919; *Angew. Chem., Int. Ed.* **2004**, *43*, 6748−6751. (c) Hof, F.; Rebek, J. *Proc. Natl. Acad. Sci. U.S.A.* **2002**, *99*, 4775−4777. (d) Rebek, J. *Heterocycles* **2000**, *52*, 493−504. (e) Körner, S. K.; Tucci, F. C.; Rudkevich, D. M.; Heinz, T.; Rebek, J. *Chem. Eur. J.* **2000**, *6*, 187−195. (f) Kang, J. M.; Santamaria, J.; Hilmersson, G.; Rebek, J. *J. Am. Chem. Soc.* **1998**, *120*, 7389−7390. (g) Kang, J. M.; Hilmersson, G.; Santamaria, J.; Rebek, J. *J. Am. Chem. Soc.* **1998**, *120*, 3650−3656.

(8) Selected examples for macrocycles deposited on surfaces and studied with scanning probe microscopy: (a) Kromer, J.; Rios-Carreras, I.; Fuhrmann, G.; Musch, C.; Wunderlin, M.; Debaerdemaeker, T.; Mena-Osteritz, E.; Bäuerle, P. *Angew. Chem.* **2000**, *112*, 3623−3628; *Angew. Chem., Int. Ed.* **2000**, *39*, 3481−3486. (b) Mena-Osteritz, E.; Bäuerle, P. *Adv. Mater.* **2001**, *13*, 243−246. (c) Laitenberger, P.; Claessens, C. G.; Kuipers, L.; Raymo, F. M.; Palmer, R. E.; Stoddart, J. F. *Chem. Phys. Lett.* **1997**, *279*, 209−214. (d) Menozzi, E.; Pinalli, R.; Speets, E. A.; Ravoo, B. J.; Dalcanale, E.; Reinhoudt, D. N. *Chem. Eur. J.* **2004**, *10*, 2199−2206. (e) Levi, S. A.; Guatteri, P.; van Veggel, F. C. J. M.; Vancso, G. J.; Dalcanale, E.; Reinhoudt, D. N. *Angew. Chem.* **2001**, *113*, 1945−1948; *Angew. Chem., Int. Ed.* **2001**, *40*, 1892−1896. Selected examples for self-assembled metallo-supramolecular species: (f) Semenov, A.; Spatz, J. P.; Möller, M.; Lehn, J.-M.; Sell, B.; Schubert, D.; Weidl, C. H.; Schubert, U. S. *Angew. Chem.* **1999**, *111*, 2701−2705; *Angew. Chem., Int. Ed.* **1999**, *38*, 2547−2550. (g) Williams, M. E.; Hupp, J. T. *J. Phys. Chem. B* **2001**, *105*, 8944−8950. (h) Ziener, U.; Lehn, J.-M.; Mourran, A.; Möller, M. *Chem. Eur. J.* **2002**, *8*, 951−957. (i) Dmitriev, A.; Spillmann, H.; Lin, N.; Barth, J. V.; Kern, K. *Angew. Chem.* **2003**, *115*, 2774−2777; *Angew. Chem., Int. Ed.* **2003**, *42*, 2670−2673. (j) Wouters, D.; Höppener, S.; Lunkwitz, R.; Chi, L.; Fuchs, H.; Schubert, U. S. *Adv. Funct. Mater.* **2003**, *13*, 277−280. (k) Tominaga, M.; Suzuki, K.; Kawano, M.; Kusukawa, T.; Ozeki, T.; Sakamoto, S.; Yamaguchi, K.; Fujita, M. *Angew. Chem.* **2004**, *116*, 5739−5743; *Angew. Chem., Int. Ed.* **2004**, *43*, 5621−5625. Examples for intertwined species on surfaces: (l) Samori, P.; Jäckel, F.; Ünsal, O.; Godt, A.; Rabe, J. P. *ChemPhysChem* **2001**, *2*, 461−464. (m) Liu, Y.; Li, L.; Zhang, H.-Y.; Zhao, Y.-L.; Wu, X. *Macromolecules* **2002**, *35*, 9934−9938. (n) Liu, Y.; Zhao, Y.-L.; Zhang, H.-Y.; Song, H.-B. *Angew. Chem.* **2003**, *115*, 3382−3385; *Angew. Chem., Int. Ed.* **2003**, *42*, 3260−3263.

(9) For reviews on scanning probe microscopic techniques, see: (a) De Feyter, S.; Gesquière, A.; Abdel-Mottaleb, M. M.; Grim, P. C. M.; De Schryver, F. C.; Meiners, C.; Sieffert, M.; Valiyaveetil, S.; Müllen, K. *Acc. Chem. Res.* **2000**, *33*, 520−531. (b) Michl, J.; Magnery, T. F. *Proc. Natl. Acad. Sci. U.S.A.* **2002**, *99*, 4788−4792. (c) Mena-Osteritz, E. *Adv. Mater.* **2002**, *14*, 609−616. (d) De Feyter, S.; De Schryver, F. C. *Chem. Soc. Rev.* **2003**, *32*, 139−150.

(10) (a) Safarowsky, C.; Merz, L.; Rang, A.; Broekmann, P.; Herrmann, B.; Schalley, C. A. *Angew. Chem.* **2004**, *116*, 1311−1314; *Angew. Chem., Int. Ed.* **2004**, *43*, 1291−1294. (b) Safarowsky, C.; Wandelt, K.; Broekmann, P. *Langmuir* **2004**, *20*, 8261−8269. (c) Safarowsky, C.; Rang, A.; Schalley, C. A.; Wandelt, K.; Broekmann, P. *Electrochim. Acta*, in press.

(11) Gong, J.-R.; Wan, L.-J.; Yuan, Q.-H.; Bai, C.-L.; Jude, H.; Stang, P. J. *Proc. Natl. Acad. Sci. U.S.A.* **2005**, *102*, 971−974.

(12) (a) Yoshimoto, S.; Suto, K.; Itaya, K.; Kobayashi, N. *Chem. Commun.* **2003**, 2174−2175. (b) Griessl, S.; Lackinger, M. Edelwirth, M.; Hietschold, M.; Hekcl, W. M. *Single Mol.* **2002**, *3*, 25−31. (c) Huskens, J.; Mulder, A.; Auletta, T.; Nijhuis, C. A.; Ludden, M. J. W.; Reinhoudt, D. N. *J. Am. Chem. Soc.* **2004**, *126*, 6784−6797.

Scheme 1. Syntheses of the Chiral, Enantiopure Ligands (*S*,*S*)-**8** and (*S*,*S*)-**11**[a]

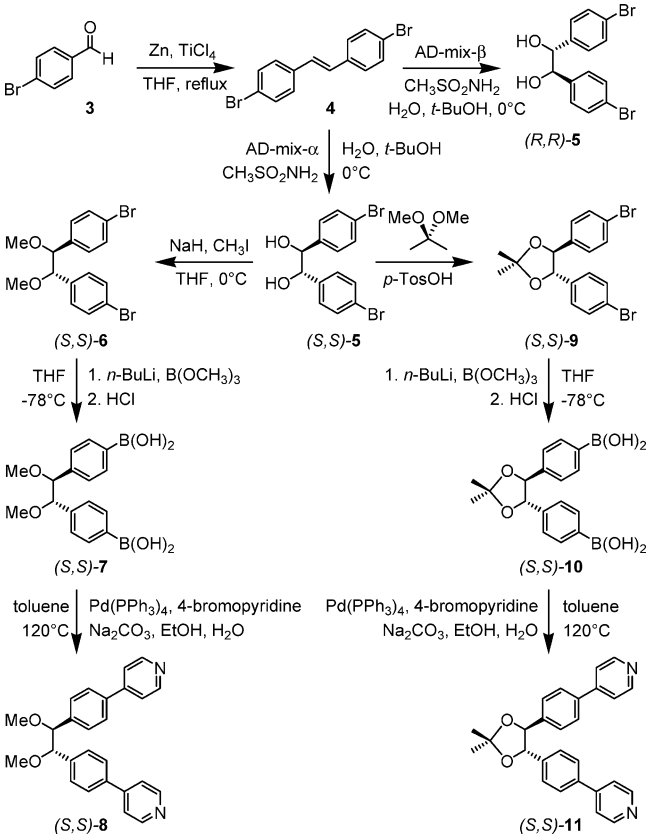

[a] The enantiomeric ligand (*R*,*R*)-**8** was synthesized similarly starting with an initial oxidation of **4** with AD-mix-β. The subsequent reaction steps were identical to those of the (*S*,*S*)-enantiomer and thus are not repeated in the scheme.

copper surface leading to the formation of a chiral electrode surface. The experimental studies are complemented with density functional theory calculations in order to gain insight into the rhombs' structures and energetics as well as to assist the interpretation of the STM images. By combining different methods for their characterization, data on the rhombs are collected which in part overlaps, and thus different methods mutually support each other. However, the methods applied here are also complementary to each other and each one adds additional details to the overall understanding of the chemical behavior of the rhombs.

Results and Discussion

Synthesis of Chiral, Enantiopure Ligands. The synthesis of the enantiopure rhombs **1a**,**b** and **2a**,**b** started from 4-bromobenzaldehyde **3** (Scheme 1) which was reductively coupled under McMurry conditions[13] to yield *trans*-4,4′-dibromostilbene **4** in nearly quantitative yield. Compound **4** was converted under the well-established Sharpless asymmetric dihydroxylation conditions[14] to yield both enantiomeric 1,2-bis(4-bromophenyl)-ethane-1,2-diols (*S*,*S*)-**5** and (*R*,*R*)-**5**, when **4** was treated with either AD-mix-α or AD-mix-β, respectively, in water/*tert*-butyl alcohol in the presence of methanesulfonamide at a temperature of 0 °C. The enantioselectivities were highly satisfactory with more than 99% ee as determined by usual chromatographic purification on a Chiralpak AD-H chiral stationary phase. The free alcohols (*S*,*S*)-**5** and (*R*,*R*)-**5** were methylated by deprotonation of the hydroxyl groups with NaH followed by nucleophilic substitution with iodomethane to give (*S*,*S*)-**6** and (*R*,*R*)-**6**, respectively. The attachment of the two pyridine moieties turned out to be somewhat difficult to achieve. Best results were finally obtained by employing the sequence given in Scheme 1. First, the bromides were replaced by boronic acid groups to yield (*S*,*S*)-**7** and (*R*,*R*)-**7**. The lithium bromide exchange was followed by treatment with trimethylborate. Subsequent hydrolysis of the corresponding boronic ester intermediates provided the boronic acid derivatives (*S*,*S*)-**7** and (*R*,*R*)-**7** in 74% and 80% yields, respectively. The $Pd(PPh_3)_4$-catalyzed Suzuki coupling[15] of (*S*,*S*)-**7** and (*R*,*R*)-**7** with the 4-bromopyridine hydrochloride proceeded uneventfully in toluene in the presence of a large excess of Na_2CO_3 and afforded the corresponding pyridine compounds in good yields of 87% for (*S*,*S*)-**8** and 85% for (*R*,*R*)-**8**. With an analogous procedure, (*S*,*S*)-**11** was available from (*S*,*S*)-**9** which can be easily obtained from intermediate (*S*,*S*)-**5** by ketal formation with 2,2-dimethoxy propane and a trace of *p*-toluenesulfonic acid, when the resulting methanol is removed in a Dean−Stark trap.

Synthesis of Enantiopure Rhombs. The preparation of rhombs **1a**,**b** and **2a**,**b** was realized according to the procedure originally developed by Fujita et al. for the self-assembly of metallo-supramolecular squares (Scheme 2).[16] A solution of ethylenediamine palladium nitrate in H_2O−methanol (1:1) was added to a solution of the enantiopure bispyridine ligand in methanol, and the resulting mixture was stirred for 15 h at 0 °C. A clear solution was obtained with trace amounts of some solid, which was filtered off. The filtrate was concentrated in vacuo to dryness, and the remaining precipitate was redissolved in methanol. Again, some insoluble material was removed by filtration, and the filtrate was concentrated. The analytically homogeneous cages **1a** and **2a** were obtained as slightly gray powders. Similarly, **1b** and **2b** were prepared from ethylenediamine platinum nitrate. It should be noted that the Pt rhombs are more easily soluble in methanol than the Pd rhombs, which require the addition of a small amount of water to the methanol solution.

CD Spectroscopy. CD spectra were recorded for the pair of enantiomeric ligands (*S*,*S*)-**8** and (*R*,*R*)-**8** and the two rhomb enantiomers (*S*,*S*,*S*,*S*)-**1a** and (*R*,*R*,*R*,*R*)-**1a** (Figure 1). Clearly, both enantiomers give mirror-symmetrical CD spectra for both substances. This is in line with a high degree of stereochemical purity as determined by chiral HPLC (see above). The positions of the CD bands attributable to the pyridine chromophore[17] are shifted to longer wavelengths in the spectra of the rhombs as compared to those of the ligands. This indicates coordination of the ligands to the metal centers.

NMR Spectroscopy. The ^{1}H NMR spectra of ligand (*S*,*S*)-**8** and the corresponding palladium rhomb (*S*,*S*,*S*,*S*)-**1a** are shown

(13) Dyker, G.; Körning, J.; Stirner, W. *Eur. J. Org. Chem.* **1998**, *149*, 9−154.
(14) Sharpless, K. B.; Amberg, W.; Bennani, Y. L.; Crispino, G. A.; Hartung, J.; Jeong, K.-s.; Kwong, H.-L.; Morikawa, K.; Wang, Z.-M.; Xu, D.; Zhang, X.-L. *J. Org. Chem.* **1992**, *7*, 2768−2771.
(15) Merk, G.; Villiger, A.; Buchecker, R. *Tetrahedron Lett.* **1994**, *35*, 3277−3280.
(16) (a) Fujita, M.; Yazaki, J.; Ogura, K. *J. Am. Chem. Soc.* **1990**, *112*, 5645−5647. Also, see: (b) von Zelewsky, A. *Coord. Chem. Rev.* **1999**, *192*, 811−825. (c) Ferrer, M.; Rodriguez, L.; Rossell, O. *J. Organomet. Chem.* **2003**, *681*, 158−166.
(17) Kleindienst, P.; Belser, P.; Wagnière, G. H. *Helv. Chim. Acta* **2003**, *86*, 950−965.

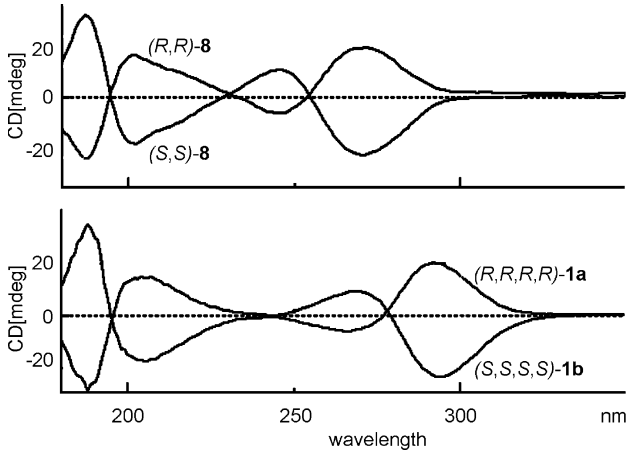

Figure 1. CD spectra of free ligands (*S*,*S*)-**8** and (*R*,*R*)-**8** (top) and Pd rhombs (*S*,*S*,*S*,*S*)-**1a** and (*R*,*R*,*R*,*R*)-**1a** (bottom).

Scheme 2. Self-Assembly of (*S*,*S*,*S*,*S*)-**1a**,**b** and (*S*,*S*,*S*,*S*)-**2a**,**b**[a]

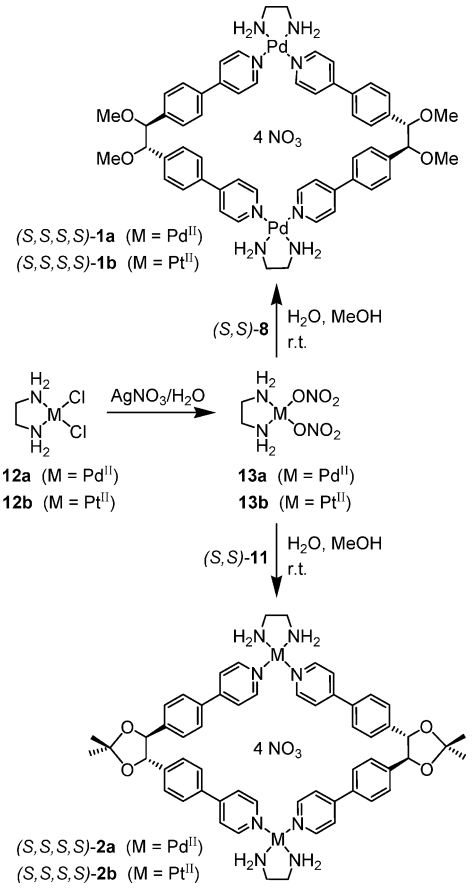

[a] (*R*,*R*,*R*,*R*)-**1a** forms under the same conditions as its all-*S* enantiomer.

in Figure 2. Both were obtained in DMSO-d_6 so that they can directly be compared. First of all, one set of sharp signals is observed for the ligand. Two of the four signals for the two AA′XX′ systems are close to each other at ca. 7.66 ppm. One of these signals shifts significantly by ca. 0.3 ppm downfield to 7.92 ppm upon complexation. We assign this signal to the ortho protons adjacent to the pyridine nitrogen atom. The downfield shift and its magnitude is typical for complexation of pyridine ligands to the (en)Pd corner. A minor complexation-induced shift of ca. 0.1 ppm to higher field is observed for the signal at 7.24 ppm, but all other signals almost exactly remain

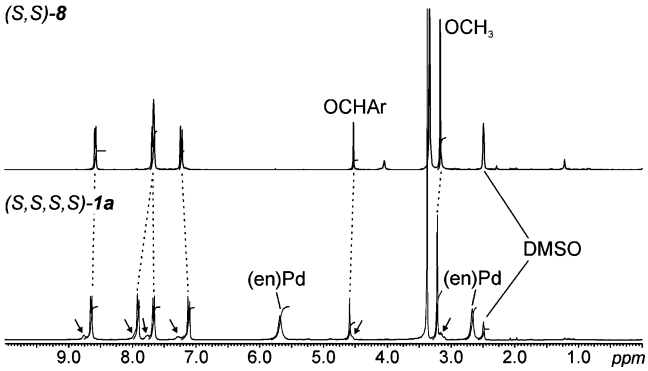

Figure 2. ^{1}H NMR spectra (DMSO-d_6, 298 K) of ligand (*S*,*S*)-**8** (top) and the corresponding Pd rhomb (*S*,*S*,*S*,*S*)-**1a**. The arrows indicate the presence of less than 10% of a second self-assembled species present in equilibrium with the rhomb (for details, see text).

at their positions upon rhomb formation. The quite simple NMR spectrum also indicates that the self-assembled product is highly symmetrical excluding the formation of, for example, short-chain oligomers, for which several sets of signals would be expected. Similarly, the ^{13}C spectra of ligand and rhomb are very similar to each other with the exception that additional signals for the (en)Pd corners appear in the latter spectrum. Nevertheless, small shifts induced by complexation are also observed here and amount to up to 4 ppm for the carbons in the ortho position relative to the pyridine nitrogen.

A closer inspection of the ^{1}H NMR spectrum reveals that each signal is accompanied by a second, much smaller signal, some of which are merely observed as a small shoulder attached to the signal for the major component. The additional signals indicate that a second, minor component (<10%) exists in equilibrium with the rhombs. Their somewhat increased complexity together with their chemical shift values which differ from that of (*R*,*R*)-**8** rules out the presence of an excess of the ligand and points to the formation of an assembly larger than the rhomb. The other rhombs behave similarly with respect to their NMR spectra.

ESI-FT-ICR Mass Spectrometric Characterization. The NMR spectra provide insight into the symmetry of the compounds under study, but it is difficult to extract exact size information from the NMR spectra, since for example macrocyclic 2:2 complexes of metal corner and chiral ligand would give rise to one set of signals as would 3:3 complexes. Mass spectrometry is complementary to the NMR experiments and can provide this information.[18] However, the intact ionization of self-assembled metallo-supramolecular species remains challenging in many cases. Fast-atom bombardment (FAB)[19] and electrospray ionization (ESI)[20] were used for ionization. Cold-spray ionization (CSI),[21] a variant of ESI operating with a cooled ion-source housing and a cooled stream of drying gas, often is

(18) For reviews, see: (a) Vincenti, M. *J. Mass Spectrom.* **1995**, *30*, 925−939. (b) Brodbelt, J. S.; Dearden, D. V. Mass Spectrometry. In *Comprehensive Supramolecular Chemistry*; Atwood, J. L., Davies, J. E. D., MacNicol, D. D., Vögtle, F., Lehn, J.-M., Ripmeester, J. A., Eds.; Pergamon: Oxford, 1996; Vol. 8, pp 567−591. (c) Przybylski, M.; Glocker, M. O. *Angew. Chem.* **1996**, *108*, 878−899; *Angew. Chem., Int. Ed. Engl.* **1996**, *35*, 806−826. (d) Brodbelt, J. S. *Int. J. Mass Spectrom.* **2000**, *200*, 57−69. (e) Schalley, C. A. *Int. J. Mass Spectrom.* **2000**, *194*, 11-**39**. (f) Lebrilla, C. B. *Acc. Chem. Res.* **2001**, *34*, 653−661. (g) Schalley, C. A. *Mass Spectrom. Rev.* **2001**, *20*, 253−309.

(19) (a) Whiteford, J. A.; Rachlin, E. M.; Stang, P. J. *Angew. Chem.* **1996**, *108*, 2643−2648; *Angew. Chem., Int. Ed. Engl.* **1996**, *35*, 2524−2529. (b) Woessner, S. M.; Helms, J. B.; Houlis, J. F.; Sullivan, B. P. *Inorg. Chem.* **1999**, *38*, 4380−4381.

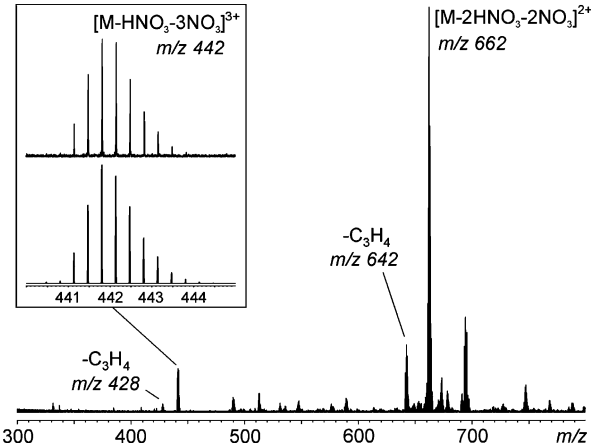

Figure 3. ESI-FT-ICR mass spectrum of a 100 μM solution of (*S*,*S*,*S*,*S*)-**2b** in methanol. The inset shows the isotope pattern of the triply charged ion [**2b**−HNO_3−$3NO_3$]$^{3+}$ obtained by experiment (top) and calculated on the basis of natural isotope abundances (bottom). The isotope pattern of the doubly charged analogue is discussed in detail in the context of Figure 4 (see below).

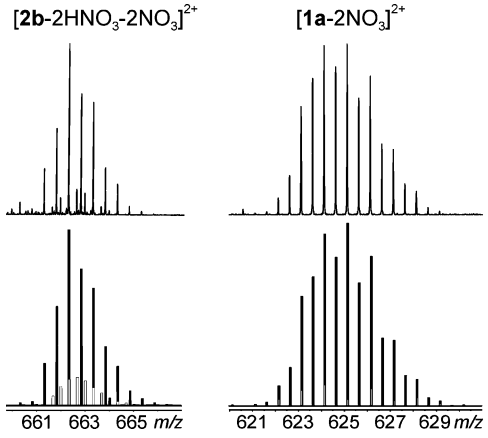

Figure 4. Top: Experimental isotope patterns for the +2 charge states of Pt rhomb [**2b**−$2HNO_3$−$2NO_3$]$^{2+}$ (left) and Pd rhomb [**1a**−$2NO_3$]$^{2+}$ (right). Bottom left: Simulated isotope pattern based on the assumption of a superposition of [**2b**−$2HNO_3$−$2NO_3$]$^{2+}$ (filled lines) with a ca. 10% contribution of a triply charged 3:3 complex (open lines). Both ions appear at the same *m*/*z* ratio but with different isotope spacings of $\Delta m = 0.5$ Da and $\Delta m = 0.33$ Da, respectively. Bottom right: Simulated isotope pattern based on the assumption of a superposition of [**1a**−$2NO_3$]$^{2+}$ (filled lines) with a 12% contribution of half a rhomb in its +1 charge state (open lines).

advantageous to achieve ionization and transfer into the gas phase of such complexes as intact species. However, the ions under study are often not completely desolvated during the CSI process causing problems in MS/MS experiments aiming at the gas-phase chemistry of the assemblies.

Figure 3 shows a typical ESI-FT-ICR mass spectrum of Pt rhomb **2b**. Since the Pt−N bonds are stronger than the Pd−N bonds, fragmentation is limited, although not completely absent. The mass spectrum shows the signal for doubly charged [**2b**−$2HNO_3$−$2NO_3$]$^{2+}$ at $m/z = 662$ as the base peak. Consequently, the ions are formed through the loss of two counterions, while the other two nitrate ions are lost together with a proton which likely originates from one of the ethylenediamine NH_2 groups. The corresponding triply charged ions [**2b**−HNO_3−$3NO_3$]$^{3+}$ are found at $m/z = 442$. Their experimental isotope pattern is not superimposed by fragments and nicely agrees with that calculated on the basis of natural abundances. Some minor signals appear between the signals for [**2b**−$2HNO_3$−$2NO_3$]$^{2+}$ with the same mass-to-charge ratio, but at peak spacings of 0.33 Da (Figure 4). They can be attributed to a triply charged ion bearing three ligands *(S,S)*-**11** and three metal corners. The observation of these triply charged ion is in excellent, even semiquantitative agreement with the finding of the minor second set of signals in the corresponding ^{1}H NMR spectra as described above for (*S*,*S*,*S*,*S*)-**1a**.

Considering the much weaker Pd−N bond, we expected to observe much more fragmentation from rhombs **1a** and **2a**. To some extent, this is indeed visible in the mass spectra which reveal enhanced intensities for fragment signals, although very soft ionization conditions have been used. Under these conditions, the ionization of the Pd compounds occurs by stripping away counterions, but the remaining nitrate anions are still present in the ions instead of deprotonating the ethylenediamine NH_2 groups. Consequently, a doubly charged ion [**1a**−$2NO_3$]$^{2+}$ is observed for rhomb **1a** at *m*/*z* 625. The increased tendency of the Pd complexes to fragment can be seen in the isotope pattern of this ion, which is superimposed by ca. 12% of the singly charged fragmentation product corresponding to half a rhomb (Figure 4).

The other rhombs behaved similarly so that we can conclude ESI-FT-ICR mass spectrometry to contribute valuable size information and—together with the NMR spectra—to provide evidence for the self-assembly of the rhombs. The combination of both also allowed the identification of the second, minor component present in solution.

Gas-Phase Reactivity. Beyond analytical characterization, FT-ICR mass spectrometry is capable of providing insight into the gas-phase reactivity of the ions under study under environment-free conditions. Often reactions can be analyzed by tandem MS experiments which cannot be examined in condensed phase.[5a,20m] To take a closer look at the behavior of the rhomb ions in the gas phase, the ions of interest were mass-selected in the FT-ICR cell and subjected to a collision-induced decay (CID) experiment. Since we expected pronounced, but not very interesting, losses of HNO_3 from ions such as [**1a**−$2NO_3$]$^{2+}$, [**2b**−$2HNO_3$−$2NO_3$]$^{2+}$ was isolated in the FT-ICR cell instead. Two problems arise: (i) To avoid superposition with the triply charged ions discussed above, only every second signal of the

(20) Selected examples: (a) Stang, P. J.; Cao, D. H.; Chen, K.; Gray, G. M.; Muddiman, D. C.; Smith, R. D. *J. Am. Chem. Soc.* **1997**, *119*, 5163−5168. (b) Manna, J.; Kuehl, C. J.; Whiteford, J. A.; Stang, P. J.; Muddiman, D. C.; Hofstadler, S. A.; Smith, R. D. *J. Am. Chem. Soc.* **1997**, *119*, 11611−11619. (c) Leize, E.; Van Dorsselaer, A.; Krämer, R.; Lehn, J.-M. *J. Chem. Soc., Chem. Commun.* **1993**, 990−993. (d) Hopfgartner, G.; Piguet, C.; Henion, J. D. *J. Am. Soc. Mass Spectrom.* **1994**, *5*, 748−756. (e) Marquis-Rigault, A.; Dupont-Gervais, A.; Van Dorsselaer, A.; Lehn, J.-M. *Chem. Eur. J.* **1996**, *2*, 1395−1398. (f) Romero, F. M.; Ziessel, R.; Dupont-Gervais, A.; Van Dorsselaer, A. *Chem. Commun.* **1996**, 551−553. (g) Marquis-Rigault, A.; Dupont-Gervais, A.; Baxter, P. N. W.; Van Dorsselaer, A.; Lehn, J.-M. *Inorg. Chem.* **1996**, *35*, 2307−2310. (h) König, S.; Brückner, C.; Raymond, K. N.; Leary, J. A. *J. Am. Soc. Mass Spectrom.* **1998**, *9*, 1099−1103. (i) Hopfgartner, G.; Vilbois, F.; Piguet, C. *Rapid Commun. Mass Spectrom.* **1999**, *13*, 302−306. (j) Ziegler, M.; Miranda, J. J.; Andersen, U. N.; Johnson, D. W.; Leary, J. A.; Raymond, K. N. *Angew. Chem.* **2001**, *113*, 755−758; *Angew. Chem., Int. Ed.* **2001**, *40*, 733−736. (k) Sautter, A.; Schmid, D. G.; Jung, G.; Würthner, F. *J. Am. Chem. Soc.* **2001**, *123*, 5424−5430. (l) Würthner, F.; Sautter, A.; Schmid, D.; Weber, P. J. A. *Chem. Eur. J.* **2001**, *7*, 894−902. (m) Schalley, C. A.; Müller, T.; Linnartz, P.; Witt, M.; Schäfer, M.; Lützen, A. *Chem. Eur. J.* **2002**, *8*, 3538−3551.

(21) (a) Sakamoto, S.; Fujita, M.; Kim, K.; Yamaguchi, K. *Tetrahedron* **2000**, *56*, 955−964. (b) Sakamoto, S.; Yoshizawa, M.; Kusukawa, T.; Fujita, M.; Yamaguchi, K. *Organic Lett.* **2001**, *3*, 1601−1604. (c) Tominaga, M.; Suzuki, K.; Kawano, M.; Kusukawa, T.; Ozeki, T.; Sakamoto, S.; Yamaguchi, K.; Fujita, M. *Angew. Chem.* **2004**, *116*, 5739−5743; *Angew. Chem., Int. Ed.* **2004**, *42*, 5621−5625. For a review, see: (d) Yamaguchi, K. *J. Mass Spectrom.* **2003**, *38*, 473−490.

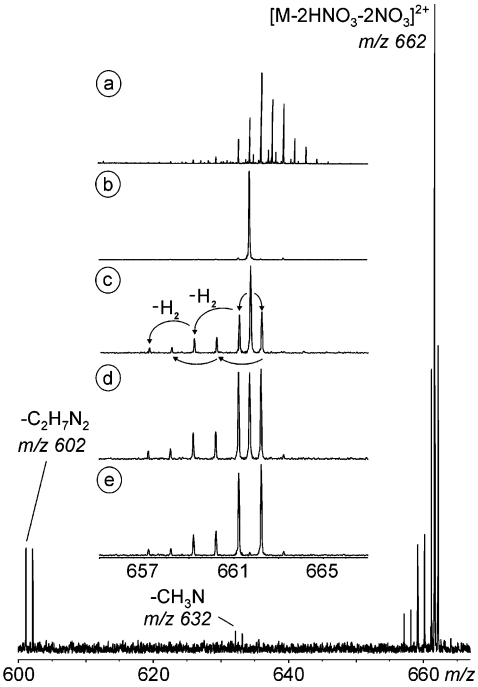

Figure 5. (a) Experimental isotope pattern of doubly charged $[\mathbf{2b}-2HNO_3-2NO_3]^{2+}$ (cf., Figure 3). (b) Isolation of the ions corresponding to the signal at *m*/*z* 661.7 which is not superimposed by the triply charged ions. (c−e) Collision-induced decay with argon as the collision gas at increasing collision energies (hydrogen-loss region only). The overview spectrum at the bottom shows the CID spectrum (c) including also the fragments at lower masses.

doubly charged species is suitable for isolation. (ii) One can expect fragmentation to yield two identical, singly charged halves. Since this fragment appears at the same *m*/*z* value, one would not be able to observe any reaction at all, when isolating an ion with an integer nominal mass-to-charge ratio. Figure 5a,b shows the solution to both problems. By mass-selecting the isotope at $m/z = 661.7$, i.e., the second of the more intense signals, the isolated ions do not contain any contribution of the triply charged species. At the same time, they either bear one ^{194}Pt and one ^{195}Pt isotope, but exclusively ^{12}C, or they contain two ^{194}Pt atoms and exactly one ^{13}C. This ensures that the *m*/*z* values of both halves differ by 0.5 mass units from the parent and by 1 mass unit from each other irrespective of the isotope composition. After isolation of the parent ion (Figure 5b), argon is pulsed into the FT-ICR cell as the collision gas. The spectra in Figure 5c−e show the results from CID experiments at increasing collision energies. The parent ion disappears in favor of two primary fragments which are formed in a 1:1 ratio and correspond to the two singly charged halves (Scheme 3). This confirms that singly charged 1:1 complexes observed in the ESI mass spectra are likely formed by fragmentation rather than ionization of 1:1 complexes already present in solution.

Some consecutive fragments are observed which are due to reactions of the coordinatively unsaturated metal ions incorporated in both fragments. First of all, two consecutive losses of molecular hydrogen are observed, for which a mechanism is shown in Scheme 3. As typically observed for many transition metal compounds in the gas phase[22] and as known from catalytic

(22) (a) Eller, K.; Schwarz, H. *Chem. Rev.* **1991**, *91*, 1121−1177. (b) Eller, K. *Coord. Chem. Rev.* **1993**, *126*, 93−147.

Scheme 3. Fragmentation Pathways for Doubly Charged $[\mathbf{2b}-2HNO_3-2NO_3]^{2+}$ [a]

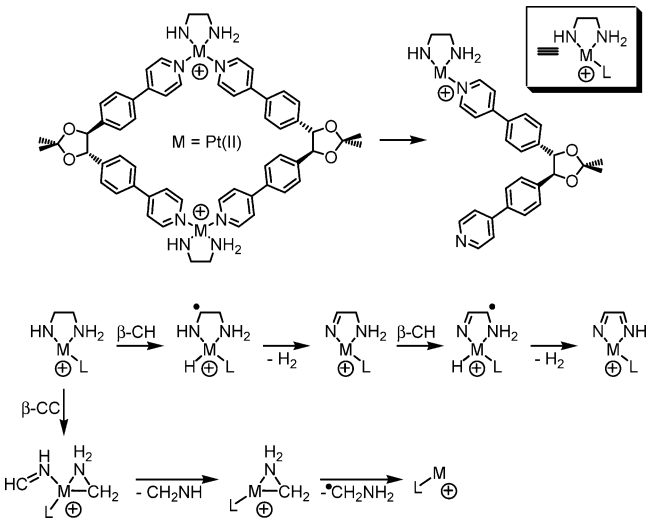

[a] The initial formation of two identical singly charged halves is followed by C−H and C−C bond activation reactions mediated by the coordinatively unsaturated metal ion.

reactions in solution involving palladium (e.g., the Heck reaction),[23] an energetically favorable β-hydrogen shift to the metal can easily occur from one of the CH_2 groups of the ethylenediamine ligand. Molecular hydrogen is then lost by combining this hydrogen with one of the nitrogen-centered hydrogen atoms. A repetition of this C−H bond activation reaction sequence leads to a diaza-metalla-cyclopentadiene structure. Instead of a β-hydrogen shift, the metal can also activate the ethylenediamine C−C bond. This is the initial step in the loss of neutral [C, H_3, N] (Figure 5) to which we tentatively assign the structure of imine, $CH_2{=}NH$ which can be followed by an additional loss of neutral [C, H_4, N] giving rise to an ethylenediamine-free complex. These experiments demonstrate the occurrence of reactions initiated by the coordinatively unsaturated metal center once the rhomb is destroyed. Since the pyridine fragment remains within the complex for the reactions discussed here, the energetic requirements for the C−H and C−C activation processes are at least qualitatively limited by the Pt−N bond dissociation energy. No indication was observed implying the pyridine ligand to be more than a pure spectator ligand during these reactions.

Electrochemical Scanning Tunneling Microscopy. It is well-known that anion layers can act as excellent templates in order to lock large and positively charged organic molecules and metal complexes to electrode surfaces.[10,24] The right balance between adsorbate−substrate interactions and the competing adsorbate−adsorbate interactions is an absolute prerequisite for an extended long-range order in such coupled anion−cation systems. Both enhanced electrostatic interactions and hydrophobic effects have been identified as driving forces for the

(23) Selected reviews on the Heck reaction: (a) Zapf, A. *Angew. Chem.* **2003**, *115*, 5552−5557; *Angew. Chem., Int. Ed.* **2003**, *42*, 5394−5399. (b) Moreno-Manas, M.; Pleixats, R. *Acc. Chem. Res.* **2003**, *36*, 638−643. (c) Soderberg, B. C. G. *Coord. Chem. Rev.* **2002**, *224*, 171−243. (d) Shibasaki, M.; Vogl, E. M. *J. Organomet. Chem.* **1999**, *576*, 1−15. (e) de Meijere, A.; Bräse, S. *J. Organomet. Chem.* **1999**, *576*, 88−110. (f) Amatore, C.; Jutand, A. *J. Organomet. Chem.* **1999**, *576*, 254−278.

(24) (a) Kunitake, M.; Batina, N.; Itaya, K. *Langmuir* **1995**, *11*, 2337−2340. (b) Ogaki, K.; Batina, N.; Kunitake, M.; Itaya, K. *J. Phys. Chem.* **1996**, *100*, 7185−7190. (c) Batina, N.; Kunitake, M.; Itaya, K. *J. Electroanal. Chem.* **1996**, *405*, 245−250.

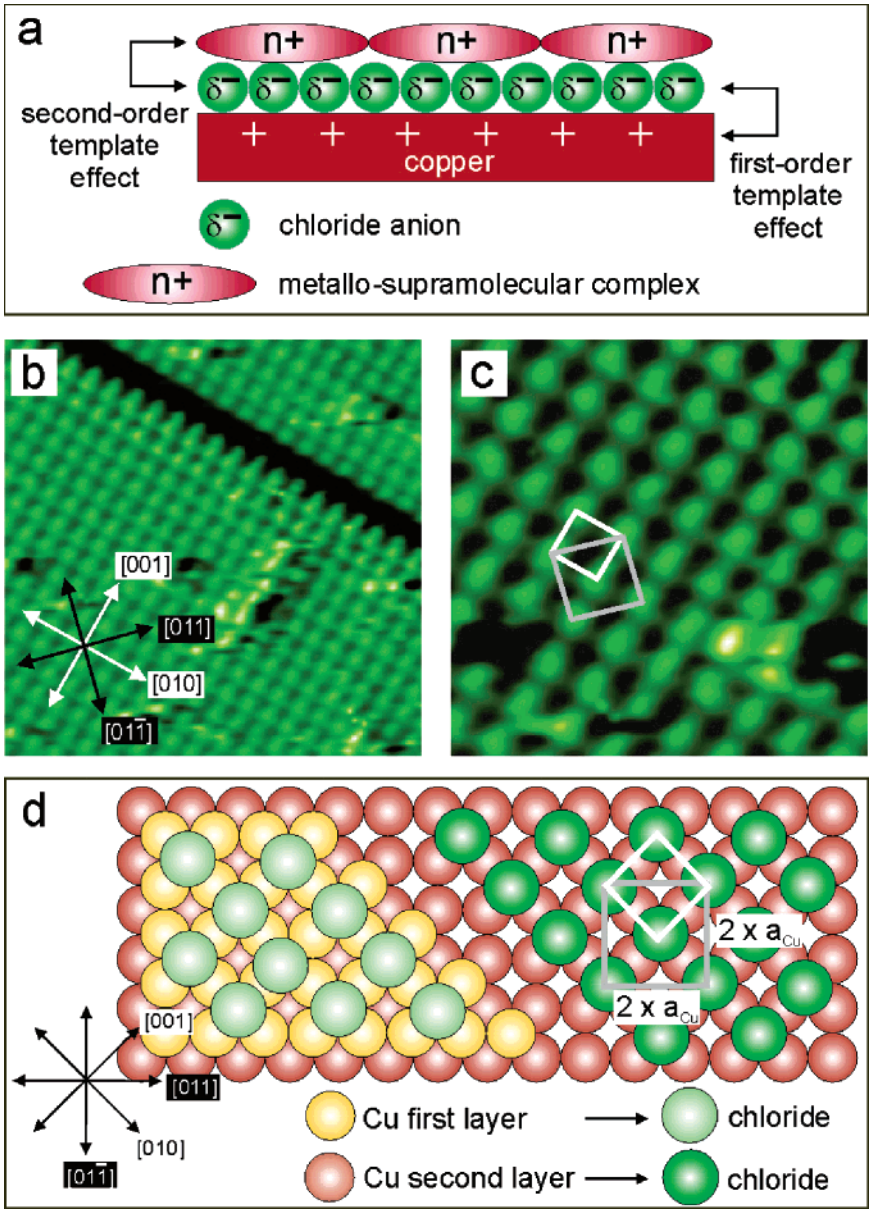

Figure 6. (a) Schematic model demonstrating the hierarchy of template effects. (b) Copper step stabilized by specifically adsorbed chloride anions, 6.4 nm × 6.4 nm, $I_t = 5$ nA, $U_{bias} = 18$ mV, $E_{work} = -400$ mV vs Ag/AgCl. (c) Atomic structure of the $(\sqrt{2} \times \sqrt{2})$R45°−Cl adlayer on Cu(100), 2.9 nm × 2.9 nm, $I_t = 5$ nA, $U_{bias} = 18$ mV, $E_{work} = -400$ mV vs Ag/AgCl. (d) Hard-sphere model of the chloride layer on Cu(100).

adsorption of these (metal)organics and their subsequent 2D ordering at the surface. The underlying principle is shown in Figure 6a.

In our experiments a positively charged Cu(100) surface exposed to diluted hydrochloric acid serves as a first-order template which transmits its 4-fold symmetry into the covering chloride layer. The resulting chloride structure can be described either by a $(\sqrt{2} \times \sqrt{2})$R45° or alternatively by a larger c(2 × 2) unit cell (Figure 6c) with an overall surface coverage of $\Theta = 0.5$ ML with respect to the copper substrate.[25]

It should be noted that surfaces do not inherently represent an electronic or geometric template structure for covering adsorbate layers. To achieve a pronounced surface template effect not only strong adsorbate−substrate interactions are required, but also a strong modulation of these interactions according to the lattice symmetry and dimensions of the substrate unit cell. A direct counterpart to the template effect of Cu(100) on the covering chloride structure can be seen in the chloride phase behavior on Au(100).[26] Although the adsorbate−substrate interactions are also strong in the latter case, one observes (quasi)hexagonal chloride layers on the *4-fold symmetric* Au(100) indicating that the elastic adsorbate−adsorbate interactions are ruling the chloride phase behavior in the absence of a strong modulation of the adsorbate−substrate interaction. Characteristically, the chloride layers undergo a compression/decompression depending on the electrode potential with resulting incommensurate phases while the highly commensurate $(\sqrt{2} \times \sqrt{2})$R45° chloride layer on Cu(100) remains

(25) (a) Magnussen, O. M. *Chem. Rev.* **2002**, *131602*, 679−725. (b) Suggs, D. W.; Bard, A. J. *J. Phys. Chem.* **1995**, *99*, 8349−8355. (c) Vogt, M. R.; Lachenwitzer, A.; Magnussen, O. M.; Behm, R. J. *Surf. Sci.* **1998**, *399*, 49−69. (d) Magnussen, O. M.; Vogt, M. R. *Phys. Rev. Lett.* **2000**, *85*, 357−360. (e) Magnussen, O. M.; Zitzler, L.; Gleich, B.; Vogt, M. R.; Behm, R. J. *Electrochim. Acta* **2001**, *46*, 3725−3733.

(26) Cuesta, A.; Kolb, D. M. *Surf. Sci.* **2000**, *465*, 310−316.

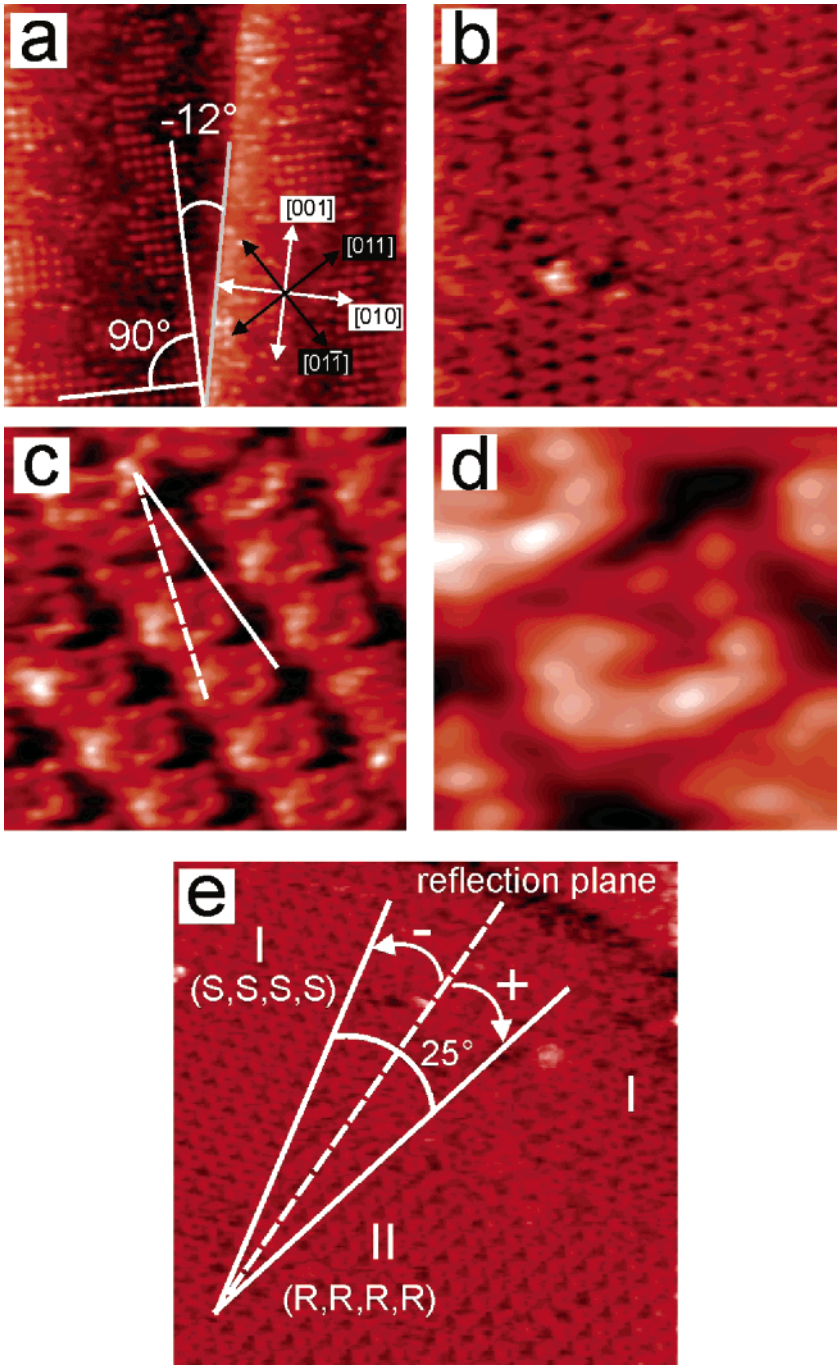

Figure 7. (a) Ordered domains of the supramolecular metal complex **1b** on the chloride template layer, 60 nm × 60 nm, $I_t = 0.1$ nA, $U_{bias} = 208$ mV, $E_{work} = -400$ mV vs Ag/AgCl. (b) 33.5 nm × 33.5 nm, $I_t = 0.1$ nA, $U_{bias} = 150$ mV, $E_{work} = -408$ mV vs Ag/AgCl. (c) Molecular packing within ordered domains, 11.8 nm × 11.8 nm, $I_t = 0.1$ nA, $U_{bias} = 150$ mV, $E_{work} = -408$ mV vs Ag/AgCl. (d) Submolecular resolution of the supramolecular metal complex, 4.1 nm × 4.1 nm, $I_t = 0.1$ nA, $U_{bias} = 145$ mV, $E_{work} = -408$ mV vs Ag/AgCl. (e) Appearance of mirror domains after exposing the substrate to a racemic mixture of rhomboids, 35 nm × 35 nm, $I_t = 0.1$ nA, $U_{bias} = 295$ mV, $E_{work} = -400$ mV vs Ag/AgCl.

stable against changes of the electrode potential in the potential regime between copper dissolution and the onset of the hydrogen evolution reaction.[25]

As typical for strongly adsorbing species also the surface morphology on a larger length scale is altered by the presence of the chloride layer on Cu(100) (Figure 6b). Copper steps are oriented parallel to the close-packed chloride rows[25] which are rotated by 45° with respect to the main symmetry substrate directions (Figure 6d).

After preparation and characterization of this negatively charged chloride layer, the positively charged analytes can be deposited as a second layer on top of the chloride lattice which takes the role of a secondary template and binds the metallo-supramolecular macrocycles into the desired flat orientation, thus overruling a pure self-assembly between these species.

When the enantiomerically pure metallo-supramolecular rhomb (*S*,*S*,*S*,*S*)-**1b** is added to the pure supporting electrolyte, an additional adlayer of **1b** is instantaneously formed on top of the $(\sqrt{2} \times \sqrt{2})$R45° chloride layer. Locally ordered patches of bright STM spots are clearly visible in Figure 7a. These spots are assigned to individual rhombs which arrange into a lattice with a square-shaped unit cell. Characteristically, the main

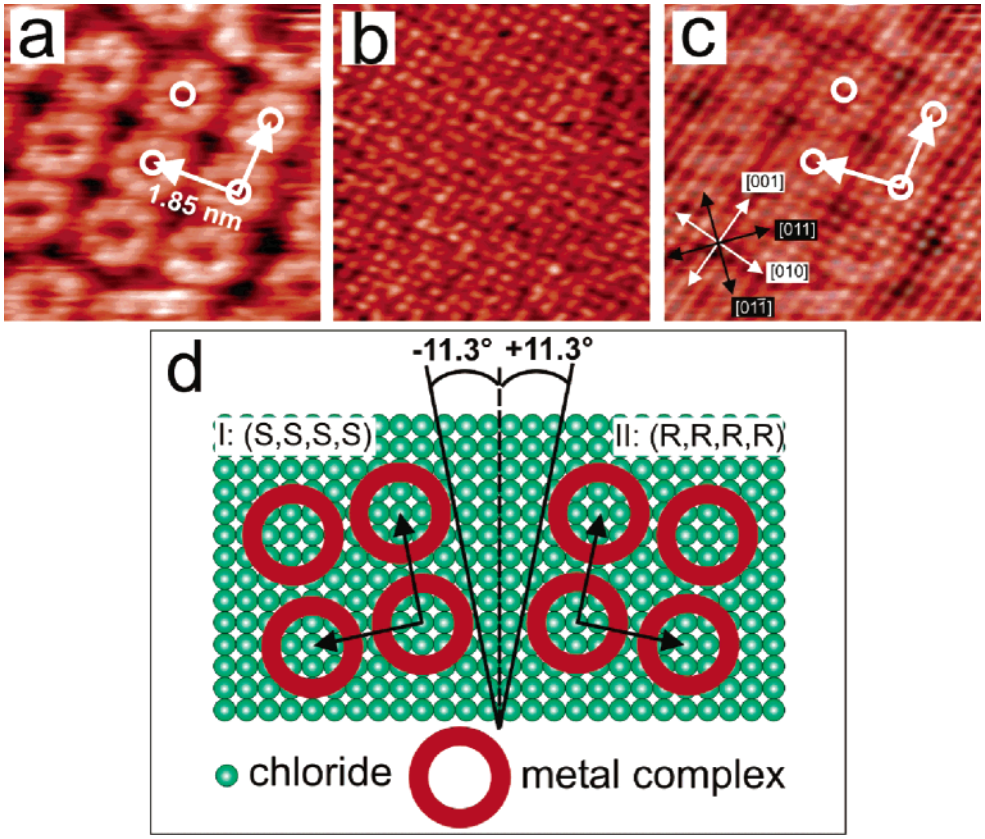

Figure 8. Correlation between the layer of rhombs **1b** and the chloride layer underneath: (a) Rhomb layer imaged under moderate tunneling conditions, 6.6 nm × 6.6 nm, I_t = 0.1 nA, U_{bias} = 100 mV, E_{work} = −400 mV vs Ag/AgCl. (b) Chloride layer imaged under more drastic tunneling conditions, 6.6 nm × 6.6 nm, I_t = 5 nA, U_{bias} = 5 mV, E_{work} = −400 mV vs Ag/AgCl. (c) Superposition of (a) and (b). (d) Hard-sphere model of the ($\sqrt{26} \times \sqrt{26}$)11.3° unit cell on the chloride lattice; only one of both mirror domains is realized due to the chirality of the metal complex.

symmetry axes of this lattice coincide neither with those of the chloride lattice (white arrows in Figure 7a) nor with those of the copper substrate (black arrows in Figure 7a). From Figure 7a one determines a characteristic angle of −12° ± 1° between substrate ⟨100⟩ directions and the lattice cell vector of the metal−organic adlayer. It should be stressed that characteristic domains with only one well-defined orientation with respect to the underlying substrate were present at the surface when enantiomerically pure rhombs were adsorbed. However, this does not hold true when a racemic mixture of these rhombs was added to the supporting electrolyte. The Pt rhombs are well suited for such an experiment, because the exchange of ligands is slow enough to allow one to carry out the measurements before the formation of statistical amounts of the meso form. In the latter case, two domains of rhombs were consistently observed in the STM experiment denoted as I and II in Figure 7e. Characteristically, their main symmetry axes enclose an angle of 25° ± 2°. It is evident that the presence of both enantiomers in the electrolyte leads to a spontaneous separation of these enantiomers at the surface resulting in enantiomerically pure domains. Please note, domain I in Figure 7e is structurally equivalent to the domain observed in Figure 7a. Both reveal the same orientation with respect to the substrate.

A closer inspection of such an enantiomerically pure domain of rhombs (Figure 7b) allows one to derive more structural details of their molecular packing at the surface. Clearly visible, the cavities of the metal complexes are oriented toward the solution phase pointing to an almost flat-lying metal complex on the chloride template layer. The molecular axes of the metallo-supramolecular complex are slightly tilted with respect to the unit cell vectors of the adlayer as indicated in Figure 7c. From the submolecular resolution presented in Figure 7c,d, the rhombic shape of the metal complex becomes evident.

The correlation of the metal−organic adlayer to the chloride lattice underneath and a precise determination of the unit cell dimensions can be performed by a systematic variation of the tunneling conditions as demonstrated in Figure 8. Moderate tunneling conditions allow us to image the metallo-supramolecular adlayer (Figure 8a), while more drastic tunneling conditions lead to its locally confined removal. This procedure provides a visualization of the intact chloride layer underneath (Figure 8b). It should be stressed that this kind of locally confined damage of the metal−organic adlayer is reversible. Retracting the STM tip from the surface by applying again moderate tunneling conditions leads to the full restoration of the adlayer of rhombs on top. From a superposition of parts a and b of Figure 8 (Figure 8c) we determine a ($\sqrt{26} \times \sqrt{26}$)-11.3° unit cell relating the adlayer of rhombs to the chloride lattice (Figure 8d). The angle of −11.3° compares quite well with the observation that the lattice vector of the metal−organic adlayer, and the step edge encloses an angle of −12° ± 1° (see above).

Even in the presence of the metal−organic layer, step edges remain oriented parallel to the close-packed chloride rows. An alternative route to describe the metal−organic adlayer is assuming a ($\sqrt{52} \times \sqrt{52}$)33.7° unit mesh which directly relates

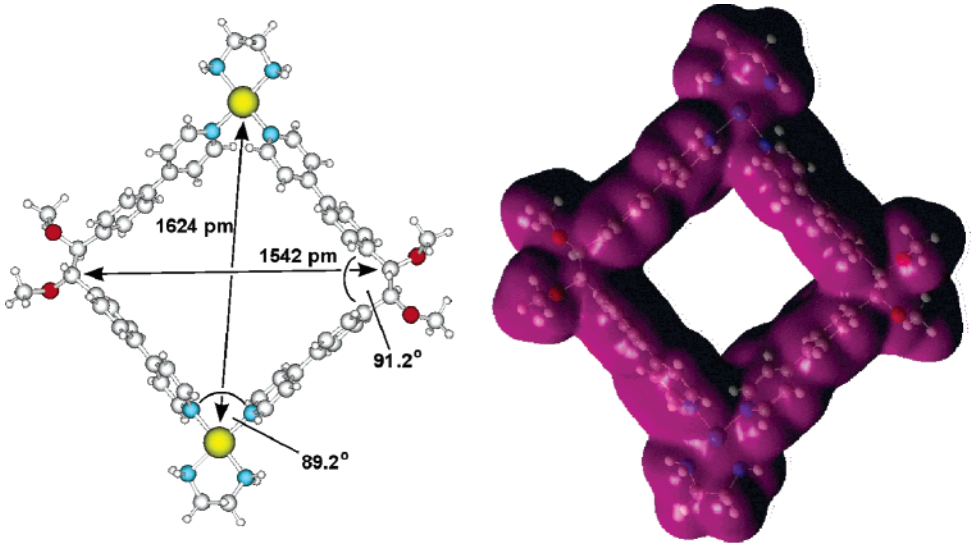

Figure 9. Optimized BP86/RI/TZVP structure of metallo-supramolecular macrocycle **1b** (left). A plot of the electronic density, which nicely displays the slightly acute angle at the two platinum corners and the somewhat obtuse angle at the methoxy-substituted corners (right).

the metal−organic adlayer to the Cu(100) substrate. The NND (nearest neighbor distance) between individual metal complexes amounts to 1.85 nm which agrees quite well with the rhomb's van der Waals diameter determined from density functional calculations (see below).

Finally, it should be noted that the stability of the surface-attached rhombs was examined by cyclic voltammetry. The rhomb adlayer turned out to be stable over the whole potential range available between hydrogen evolution at one end and copper dissolution at the other. No peaks in addition to those seen in the CV of a copper surface in HCl are observed. Consequently, no special redox chemistry of the rhombs occurs in this range. On the basis of the well-defined epitaxial relation of the chloride layer and the rhombs, one might expect that the adlayer changes, as soon as the chloride desorbs. Experimentally, this change cannot be observed, because the potential regime for chloride desorption overlaps with that of hydrogen evolution.

Density Functional Calculations. The structures of (*S*,*S*,*S*,*S*)-**1b** and (*S*,*S*,*S*,*S*)-**2b** were optimized using density functional theory. Figure 9 shows the DFT-optimized structure of **1b** in a ball-and-stick model (left; details of **2b** are available in the Supporting Information). The metal corners are quite distant from each other, i.e., the two Pt atoms are separated by ca. 1.62 nm. The distance between the two corners incorporated in the ligands is somewhat shorter and amounts to 1.54 nm. The calculated N−Pt−N angle and that between the two PyN−COMe axes are close to the expected right-angled coordination geometry and amount to 89.2° and 91.2°, respectively. From these data it is clear that 1**b** deviates only slightly from a square. This deviation from an ideal square can also be seen in the surface plot of the electron density (Figure 9, right). The geometrical data fits quite well to those obtained from the STM experiments, which provide an NND between individual metal complexes of ca. 1.85 nm in good agreement with the van der Waals diameter of the metal complex.

Beyond the overall shape and size information, the calculations also yield molecular orbitals that might be used to evaluate the submolecular features seen in the STM images. The fine structure of the STM images does even allow one to discriminate between the pairs of corners, namely, the metal corners and the methoxy-substituted corners of the macrocycle: The intensively light corners are assigned to the methoxy corners according to the slightly obtuse angles. In a simple qualitative MO picture of the electronic structure of the isolated macrocycle, one would expect that the STM experiment either probes the high-lying occupied MOs or the low-lying unoccupied MOs, if the electric current flows from the probe to the tip or vice versa, respectively. A more detailed analysis of the molecular orbitals of the isolated macrocycle **1b** revealed a remarkable separation of orbitals, which are localized on either corner (see Figures 10 and 11). The 16 highest occupied MOs are located on the methoxy corners, while the 16 low-lying unoccupied orbitals are localized on the platinum centers, although no additional localization procedure by a linear transformation of the orbitals was applied.

As the STM experiments in the present study measure a current from the adsorbed macrocycle to the tip, we expect the highest lying occupied MOs to be the most important, even though our ionization-like picture of the probe-to-tip electron transfer is certainly only a simplified model. Consequently, we would attribute the intensive light areas in the STM images to the methoxy corners. Since the low-lying unoccupied MO "band" consists exclusively of MOs with metal character, we would expect these orbitals to be probed if the current would flow from the tip to the macrocycle resulting in STM images, which highlight those metal corners that remain dark in the present images. Experiments performed with different tunneling parameters, however, lead to the conclusion that the real situation is more complex so that these conclusions should only be regarded as a first approximation. Since a detailed discussion of these results is beyond the scope of this contribution, we refrain from discussing them in detail here.

To give a reasonable estimate of the HOMO/LUMO gap in the isolated system, the orbital energies obtained with different functionals are compared in Table 1. In view of the work of Salzner et al.[27] on the dependence of the HOMO−LUMO gap

(27) Salzner, U.; Pickup, P. G.; Poirier, R. A.; Lagowski, J. B. *J. Phys. Chem. A* **1998**, *102*, 2572−2578.

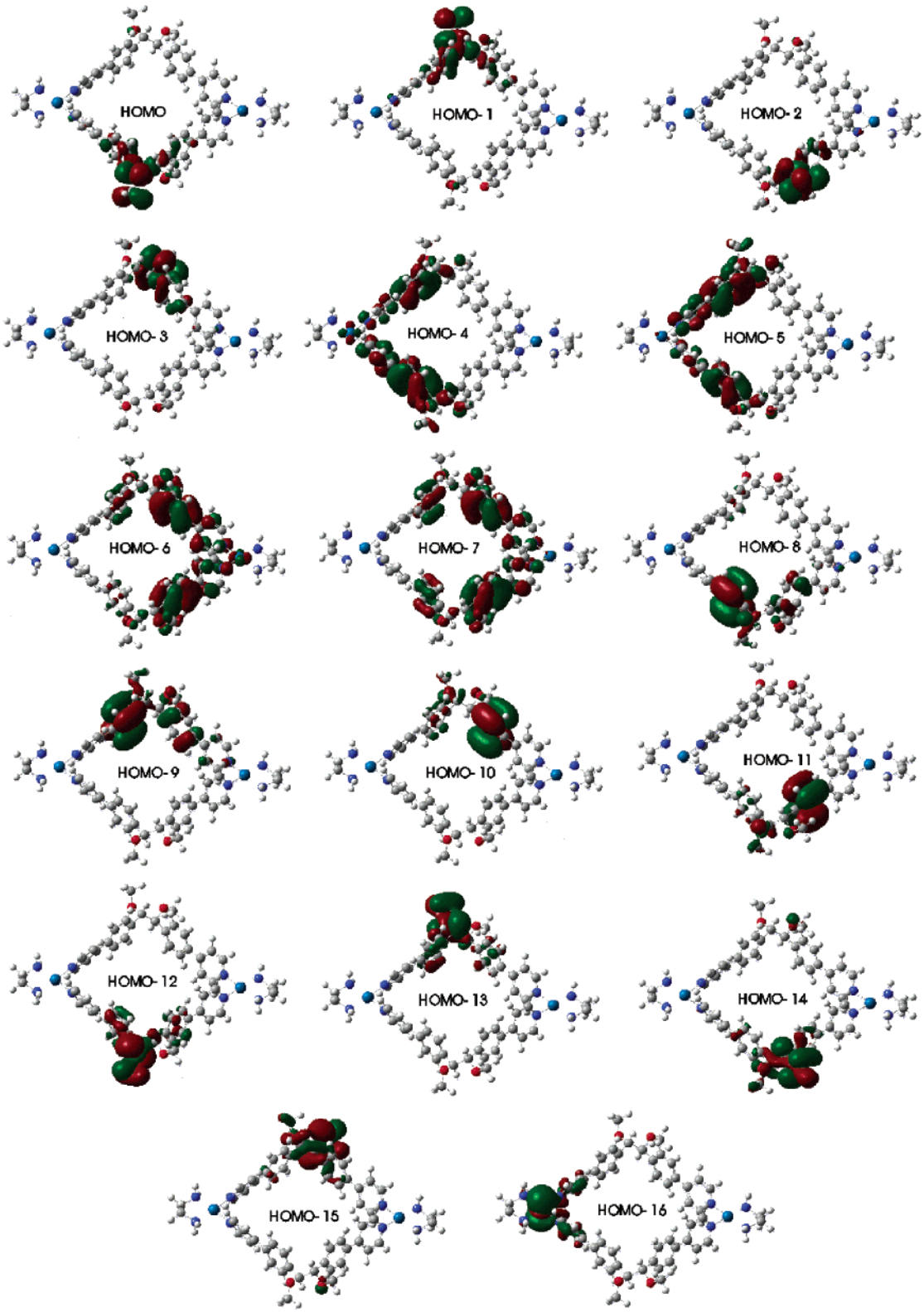

Figure 10. Highest occupied molecular orbitals of the macrocycle. Note that a dense "band" of frontier MOs exists, which solely consists of methoxy-corner MOs. The first MO with metal-character AOs is the HOMO − 16. For symmetry reasons near-degenerate pairs of orbitals exists.

on the density functional used in the calculations, we may conclude that the hybrid functional data, i.e., from either the B3LYP or PEB0 calculations, should be used instead of that generated with gradient-corrected functionals only (see Table 1 and the Experimental Section). The calculated HOMO−LUMO gap thus amounts to ca. 3.1 eV for **1b**.

The STM images show two opposite corners with little intensity, which are not symmetric as one would expect from the MO images of the isolated system. The reason for this asymmetry may be related to the underlying chloride ion template, which—for geometrical reasons—provides different environments for the two platinum corners and thus alters the

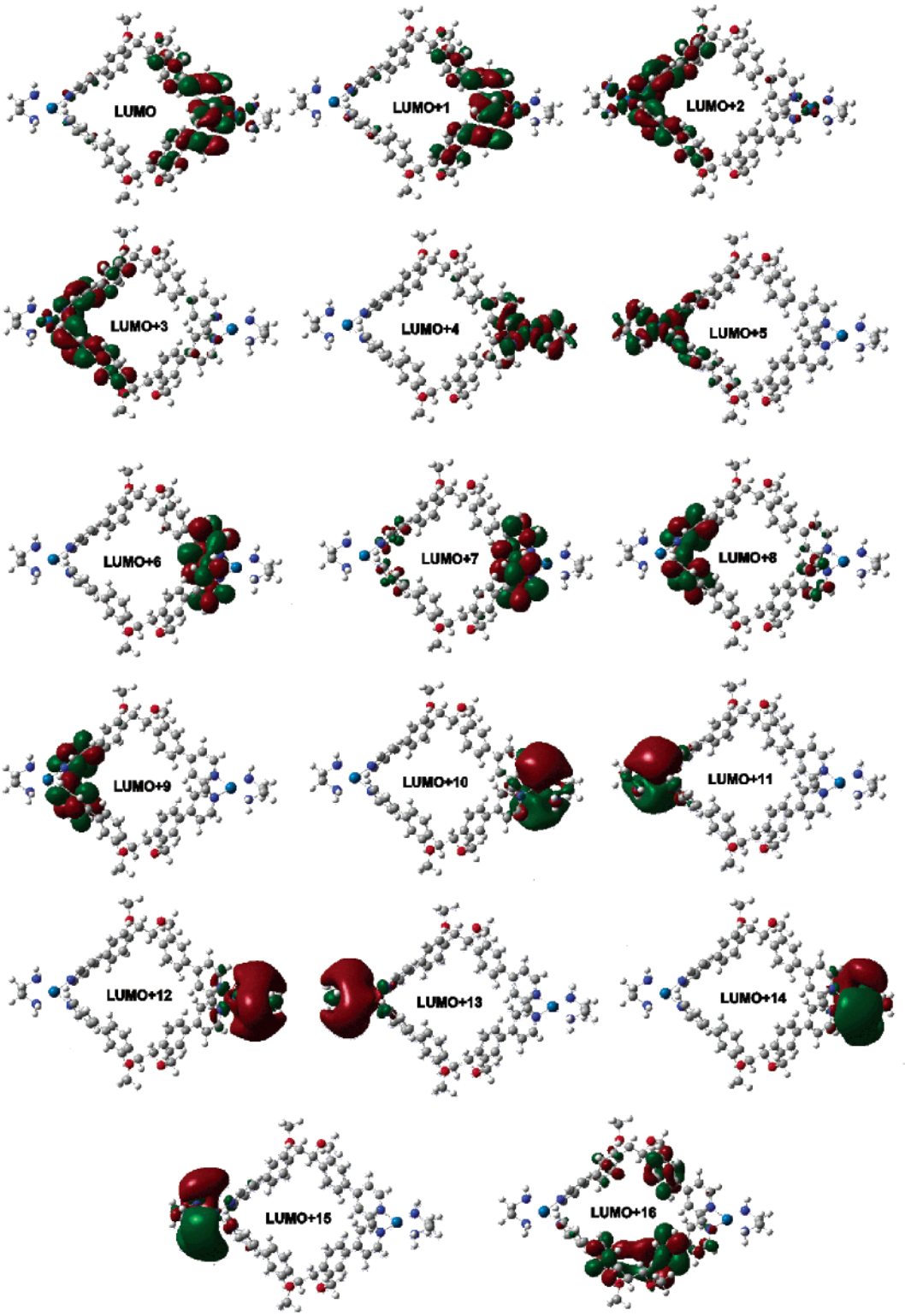

Figure 11. Low-lying unoccupied molecular orbitals of macrocycle **1b**. Note that a dense "band" of virtual frontier MOs exists, which solely consists of MOs centered at the metal corners. The first MO with AOs at the methoxy corners is the LUMO + 16. For symmetry reasons near-degenerate pairs of orbitals exists.

symmetry of the macrocycle as compared to the isolated molecule. These different environments would exert a different perturbation on the molecular orbitals of the adsorbed molecule, which in turn may explain the asymmetry of the STM images.

The calculations yield very similar results for rhomb **2b** (see, for example, Table 1). In conclusion, the DFT calculations on the isolated assemblies yield valuable insight that can tentatively be aligned with experimental observations, even though the surface and the STM tip have been neglected. It is possible to determine how the rhombs are positioned on the surface. Also, some of the details observed at submolecular resolution in the STM images can be understood from the molecular orbital calculations.

Table 1. Comparison of Orbital Energies and HOMO−LUMO Gaps Given in eV (the TZVP Basis Set Has Been Used Throughout)[a]

	BP86/RI		B3LYP		PBE0	
	1b	**2b**	**1b**	**2b**	**1b**	**2b**
HOMO − 1[b]	−11.80	−11.79	−12.73	−12.85	−13.05	−13.17
HOMO[b]	−11.79	−11.75	−12.73	−12.83	−13.05	−13.15
LUMO[b]	−10.44	−10.45	−9.63	−9.57	−9.58	−9.51
LUMO + 1[b]	−10.39	−10.42	−9.60	−9.53	−9.55	−9.46
HOMO−LUMO gap	1.35	1.30	3.10	3.26	3.47	3.64

[a] The increased gap for the hybrid functional correlates with the exact exchange admixture as expected (cf., ref 27). [b] Note that orbitals are near degenerate for symmetry reasons.

Conclusions

The synthesis of new, enantiopure, self-assembled metallo-supramolecular rhombs is reported which have been characterized in detail by NMR and CD spectroscopy in solution and by mass spectrometry in the gas phase. Collision-induced dissociation experiments under the environment-free conditions inside a mass spectrometer reveal doubly charged 2:2 complexes to fragment into two identical, singly charged halves. This fragmentation is followed by subsequent C−H and C−C bond activation reactions mediated by the coordinatively unsaturated metal center. They involve gas-phase analogues of the β-hydride shifts encountered in transition-metal-mediated catalytic processes such as the Heck reaction. Gas-phase chemistry thus provides access to processes that are difficult or impossible to study in condensed phase.

Density functional calculations provide insight not only into the geometrical features of the metallo-supramolecular rhombs but also into the shapes and energies of their molecular orbitals. Even without the use of localization procedures, a remarkable localization of molecular orbitals is observed. While the 16 highest occupied molecular orbitals are located at the corners defined by the ligands stereogenic carbon atoms, the 16 lowest unoccupied orbitals are located at the metal corners. These calculations support the interpretation of features observed in the STM experiments at submolecular resolution. The combination of methods allowed us to perform an in-depth characterization of the rhombs and their chemical properties based on which scanning tunneling microscopic experiments could be carried out.

The chiral rhombs could be adsorbed and imaged at surfaces in an electrochemical environment. One of their most conspicuous properties is certainly their chirality which manifests itself on the surface on different levels and in different qualities:[28] Adsorbing any kind of enantiopure species must inevitably lead to the formation of a local structure motif revealing a surface point chirality. This phenomenon is independent of the actual adsorption site and geometry. Even for randomly adsorbed species no mirrored chiral structure motifs can be obtained on the local level because of the inherent chirality of the adsorbed species. For the creation of the mirrored structure motif on the local level the presence of the corresponding enantiomer is always needed. As a consequence, surfaces become chiral not only on the local but also on the global level even without any lateral order of the adsorbed enantiomerically pure species.[28] Besides the phenomenon of point chirality on a global level, the adsorption of rhomboidal cages can even produce a higher level of surface chirality which is actually related to their 2D ordering as observed in our STM experiments (Figure 7a−d). This kind of organizational chirality originates from the fact that the rhomboid 2D organization "destroys" the reflection symmetry of the underlying chloride lattice. In the absence of any chiral information within the substrate or the adsorbed species both mirror domains always coexist leading to an overall nonchiral, racemic surface.[10b] Only the combination of this organizational chirality with a certain point chirality introduced by the adsorbed species produces a truly chiral surface that reveals a global organizational chirality with only one of both mirror domains present at the surface when enantiomerically pure species are adsorbed.[28] In this latter case, we end up with a truly chiral surface (chirality on a global level). This has been realized with the surface-deposited rhombs under study here and is observed in our STM experiments (Figure 7a−d). However, when we adsorb a racemic mixture of these rhombs both enantiomers are separated at the surface into enantiomerically pure domains (enantiopure 2D crystallization). In this case the organizational chirality is restricted to the local level (chiral domains). On the global level the surface remains racemic (Figure 7e).

The complexes are deposited on the surface in a flat orientation and open their cavity toward the solution phase. One future goal is to use this arrangement for the examination of host−guest chemistry at the surface by means of in situ STM. In this context, the results reported here can be seen as a crucial step toward the direct visualization of surface host−guest chemistry at electrified interfaces by means of high-resolution STM. The combination of chiral host molecules and the electrochemical environment used in the present STM experiments will be highly interesting with respect to a control of the inclusion of chiral guests through external stimuli.

Experimental Section

Syntheses. All procedures and analytical data for new compounds described here are given in the Supporting Information accompanying this article.

ESI-FT-ICR Mass Spectrometry. High-resolution ESI mass spectra and MS/MS spectra were recorded on a Bruker APEX IV Fourier transform ion cyclotron resonance (FT-ICR) mass spectrometer with an Apollo electrospray ion source equipped with an off-axis 70° spray needle. Typically, methanol, for the platinum-bearing macrocycles, and methanol/water = 5:1, for the palladium analogues, served as the spray solvents. The solutions were ca. 100 μM with respect to the concentration of the analytes. Analyte solutions were introduced into the ion source with a syringe pump (Cole-Parmers Instruments, series 74900) at flow rates of ca. 3−4 μL/min. Ion transfer into the first of three differential pumping stages in the ion source occurred through a glass capillary with 0.5 mm i.d. and nickel coatings at both ends. Ionization parameters were adjusted as follows: capillary voltage, −4.7 to −5.0 kV; endplate voltage, −3.7 to −4.3 kV; cap exit voltage, +20 to +75 V; skimmer voltages, +8 to +12 V; temperature of drying gas, 40 °C. The flows of the drying (ca. 5 psi) and nebulizer gases (ca. 5 psi) were kept in a low range. Ion intensities are somewhat sensitive to the drying gas flow. At higher flow rates, the intensities decrease. The ions were accumulated in the instruments hexapole for 0.2−3.5 s. Short accumulation times improve the abundances of intact ions in particular for the Pd complexes, because blackbody irradiation originating from the instruments walls leads to more abundant fragmentation, when older ions are examined. The ions are then introduced into the FT-ICR cell, which was operated at pressures below 10^{-10} mbar, and finally detected

(28) Barlow, S. M.; Raval, R. *Surf. Sci. Rep.* **2003**, *50*, 201−341.

by a standard excitation and detection sequence. For each measurement 32−256 scans were averaged to improve the signal-to-noise ratio.

For MS/MS experiments, the whole isotope envelopes of the ion of interest were isolated by applying correlated sweeps, followed by correlated shots to remove the undesired isotopes. The choice of the appropriate isotope is crucial (see Results and Discussion) to avoid superposition with other species. After isolation, argon was introduced into the ICR cell as the collision gas through a pulsed valve at a pressure of ca. 10^{-8} mbar. The ions were accelerated by a standard excitation protocol and detected after a 2 s pumping delay. A sequence of several different spectra was recorded at different excitation pulse attenuations in order to get at least a rough and qualitative idea of the effects of different collision energies on the fragmentation patterns.

EC-STM Experiments. All STM experiments presented in this paper have been performed using a home-built STM setup.[29] Prior to each STM experiment, the copper substrate needs to be treated by an electrochemical etching procedure in order to remove the native oxide layer that is ineluctably formed in air. For this purpose, the Cu(100) sample (MaTeck company, Jülich, Germany) is immersed into 50% orthophosphoric acid before the copper dissolution reaction is started by applying an anodic potential of 2 V between the copper sample and a platinum foil for about 20−40 s. The tunneling tips used in our experiments were electrochemically etched from 0.25 mm tungsten wire in 2 M KOH solution and subsequently isolated by passing the tip through a drop of hot-glue. For all solutions, high-purity water (Milli-Q purification system >18 MΩ·cm, TOC < 4 ppb) is used. All electrolyte solutions need to be deoxygenated with oxygen-free argon gas several hours before use. All potentials given in this paper refer to an internal Ag/AgCl reference electrode. A chloride precovered Cu(100) surface serves as the template for the adsorption of the supramolecular metal complexes. Therefore, STM measurements were first performed in the pure supporting electrolyte (10 mM HCl). The next preparation step consists of the exchange of the pure supporting electrolyte by a solution also containing the supramolecular metal complex. It is crucial not to lose potential control during this procedure. The potential window for such an exchange procedure lies in the double-layer regime between −300 and −400 mV.

Calculations. For all density functional calculations, we used the density functional programs provided by the Turbomole 5.6 suite.[30] Results were obtained from a restricted Kohn−Sham optimization of the 4-fold positively charged macrocycle (see Figure 6), in which we employed the Becke−Perdew functional dubbed BP86[31,32] as implemented in Turbomole. This functional is well-established for the calculation of reliable structural parameters of transition metal complexes.[33]

In connection with this functional we applied the resolution-of-the-identity (RI) density-fitting technique.[34] We used Ahlrichs' TZVP basis set[35] featuring a valence triple-ζ basis with polarization functions on all atoms. For the platinum atom we applied an effective core potential from the Stuttgart group[36] as implemented in Turbomole, which also takes care of a suitable description of scalar-relativistic effects on platinum.

Because of the self-interaction error, the band gap is known to be largely dependent on the density functional chosen.[27] We therefore employed apart from the pure functional BP86 the well-known hybrid functionals B3LYP[37] and PBE0[38] in single-point calculations on the BP86/RI/TZVP-optimized structure. These two hybrid functionals incorporate 20% and 25% Hartree−Fock-type exact exchange, which, from a pragmatic point of view, may be utilized to correct for the wrong behavior of the standard density functionals. Salzner et al.[27] advocate the use of 30% exact exchange in order to reproduce experimental band gaps. We, however, refrain from modifying the standard hybrid functionals as it is also known that energy splittings of different spin states would require a reduced exact exchange admixture.[33c,39]

The molecular orbitals (MOs) obtained for the macrocycle (136 atoms) in a TZVP basis require huge computer resources for the plotting, which are beyond our present hardware facilities. However, for pure inspection, these orbitals cannot be distinguished from orbitals obtained in a smaller double-ζ basis, which we therefore used for the orbital plots obtained with the Gaussview package.[40]

Acknowledgment. We are grateful to the Deutsche Forschungsgemeinschaft (DFG), in particular the Sonderforschungsbereich 624, and the Fonds der Chemischen Industrie (FCI) for funding. C.A.S. acknowledges a Heisenberg fellowship from the DFG; C.A.S. and M.R. thank the FCI for Dozentenstipendien. N.J. thanks the KOSEF (Grant No. R02-2002-000-00128-0 of the Basic Research Program), the CMDS, and Korea University for the financial support. S.Y.K., K. S. J., and W.S.S. are grateful for the B.K.21 fellowship. N.J. also thanks Prof. Karl Heinz Doetz and the DFG for the opportunity to visit the University of Bonn.

Supporting Information Available: Synthetic procedures, analytical data, theoretical details for **2b**, and copies of ^{1}H and ^{13}C NMR spectra for intermediates of ligand synthesis and rhomb **1a** (PDF). This material is available free of charge via the Internet at http://pubs.acs.org.

JA053781I

(29) Wilms, M.; Kruft, M.; Bermes, G.; Wandelt, K. *Rev. Sci. Instrum.* **1999**, *70*, 3641−3650.
(30) Ahlrichs, R.; Bär, M.; Häser, M.; Horn, H.; Kölmel, C. *Chem. Phys. Lett.* **1989**, *162*, 165−169.
(31) Perdew, J. P. *Phys. Rev. B* **1986**, *33*, 8822−8824.
(32) Becke, A. D. *Phys. Rev. A* **1988**, *38*, 3098−3100.
(33) (a) Koch, W.; Holthausen, M. C. *A Chemist's Guide to Density Functional Theory*; Wiley-VCH: Weinheim, Germany, 2000. (b) Reiher, M.; Neugebauer, J.; Hess, B. A. *Z. Phys. Chem.* **2003**, *217*, 91−103. (c) Reiher, M.; Salomon, O.; Hess, B. A. *Theor. Chem. Acc.* **2001**, *107*, 48−55.
(34) (a) Eichkorn, K.; Treutler, O.; Öhm, H.; Häser, M.; Ahlrichs, R. *Chem. Phys. Lett.* **1995**, *240*, 283−290. (b) Eichkorn, K.; Weigend, F.; Treutler, O.; Ahlrichs, R. *Theor. Chem. Acc.* **1997**, *97*, 119−124.
(35) Schäfer, A.; Huber, C.; Ahlrichs, R. J. *Chem. Phys.* **1994**, *100*, 5829−5835.
(36) Andrae, D.; Häussermann, U.; Dolg, M.; Stoll, H.; Preuss, H. *Theor. Chim. Acta* **1990**, *77*, 123−141.
(37) (a) Becke, A. D. *J. Chem. Phys.* **1993**, *98*, 5648−5652. (b) Stephens, P. J.; Devlin, F. J.; Chabalowski, C. F.; Frisch, M. J. *J. Phys. Chem.* **1994**, *98*, 11623−11627.
(38) (a) Perdew, J.; Ernzerhof, M.; Burke, K. J. *Chem. Phys.* **1996**, *105*, 9982−9985. (b) Perdew, J. P.; Burke, K.; Ernzerhof, M. *Phys. Rev. Lett.* **1996**, *77*, 3865−3868.
(39) Reiher, M. *Inorg. Chem.* **2002**, *41*, 6928−6935.
(40) *GaussView03*; Gaussian, Inc.: Wallingford, CT, 2004.